



OPEN ACCESS

EDITED BY

Julfikar Haider,
Manchester Metropolitan University,
United Kingdom

REVIEWED BY

Junchao Wei,
Nanchang University, China
Mena Krishnan,
University of Nebraska Medical Center,
United States

*CORRESPONDENCE

Fu-Xiang Song,
✉ songfuxiang@lzu.edu.cn
Bin Liu,
✉ liubkq@lzu.edu.cn

RECEIVED 18 February 2025

ACCEPTED 16 April 2025

PUBLISHED 28 April 2025

CITATION

Zhao X-Z, Shi N-Y, Chen Q, Xing Y, Guo Y-Z,
He M-Z, Song F-X and Liu B (2025) An
intelligent digital guide plate for visual
inspection of seating and dynamic balance.
Front. Mater. 12:1578888.
doi: 10.3389/fmats.2025.1578888

COPYRIGHT

© 2025 Zhao, Shi, Chen, Xing, Guo, He, Song
and Liu. This is an open-access article
distributed under the terms of the [Creative
Commons Attribution License \(CC BY\)](#). The
use, distribution or reproduction in other
forums is permitted, provided the original
author(s) and the copyright owner(s) are
credited and that the original publication in
this journal is cited, in accordance with
accepted academic practice. No use,
distribution or reproduction is permitted
which does not comply with these terms.

An intelligent digital guide plate for visual inspection of seating and dynamic balance

Xiang-Zhe Zhao, Nai-Yu Shi, Qian Chen, Yue Xing,
Yan-Zhu Guo, Ming-Zhu He, Fu-Xiang Song* and Bin Liu*

Hospital/School of Stomatology, Lanzhou University, Lanzhou, China

The aim of the present study was to develop an intelligent digital planting guide plate to achieve precise positioning and dynamic balance of the guide plate with visual real-time monitoring. To achieve this, Mechanoluminescence (ML) materials ($\text{BaSi}_2\text{O}_2\text{N}_2: \text{Eu}^{2+}$, BSON) was innovatively incorporated into methyl methacrylate (MAA) resin, forming BM composite materials with varying BSON doping concentrations (2 wt%, 4 wt%, 8 wt%, 16 wt% and 32 wt%) using mechanical blending, after 3D printing MMA was changed to Polymethyl methacrylate (PMMA). The intelligent guide plate was successfully fabricated via 3D printing technology, followed by a randomized clinical trial involving 50 patients. The successful integration of BSON into MAA was confirmed through scanning electron microscopy (SEM), X-ray diffraction (XRD), Fourier-transform infrared spectroscopy (FTIR), and X-ray photoelectron spectroscopy (XPS). Notably, the BM4 composite exhibited significantly enhanced mechanical properties, with an increase of 353.81% in elastic modulus, 64.52% in load-bearing capacity, and 70.19% in bending strength compared to pure PMMA. Additionally, BM4 demonstrated superior hydrophilicity and exceptional biocompatibility. Further, BM4 displayed pronounced mechanoluminescence in response to mechanical stress. The clinical accuracy of BM composite material intelligent guide plate was validated through a clinical study involving 50 patients implant placement with BM composite surgical guides. There was no significant difference between the BM composite material intelligent guide plate and the traditional guide plate, confirming its clinical feasibility. This study provides a precise and minimally invasive solution for oral implant restoration and is of significant importance in advancing the development of digital medical technology.

KEYWORDS

mechanoluminescence, intelligent digital planting guide, visual inspection, mechanical properties, biocompatibility

1 Introduction

Numerous oral diseases, including caries, periodontal disease, and trauma, can result in dental defects (Peres et al., 2019). These defects not only impact occlusion, mastication, and feeding, but also contribute to disorders of the stomatognathic system and potentially influence systemic health (Beck et al., 2014). According to the fourth oral health epidemiological survey, the prevalence of dental defects reached 84.4%,

while the restoration rate remained at only 41.6% (Zhi et al., 2018), highlighting the significant challenge of dental defect management. At present, the primary clinical approaches for dental defect restoration include removable partial dentures, fixed bridge restorations, and dental implants (Peng et al., 2021). Among these approaches, implant-based restoration has gained preference among both practitioners and patients due to its benefits, including the preservation of adjacent teeth, improved aesthetics, and superior restoration of masticatory function (Li et al., 2023). At the same time, with ongoing socioeconomic development and supportive national policies, the demand for implant-based restorations is increasing. Consequently, dental professionals are confronted with significant challenges in meeting this growing need.

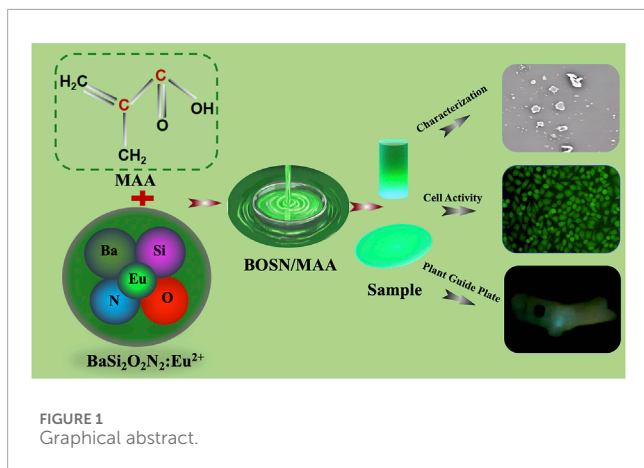
During the implant restoration process, the precise placement of the implant in the optimal three-dimensional position within the alveolar ridge is a critical determinant of success. The precision of this placement is intricately linked to the long-term clinical success rate (Nulty, 2024). In clinical practice, oral implantologists mainly choose between “free-hand” implant placement and digitally guided implant placement. Digitally guided implantation has been shown to enhance surgical precision, mitigate surgical risks, and alleviate patient discomfort (Abad-Coronel et al., 2024). As a result, an increasing number of oral implant surgeons are adopting digitally guided implantation as a preferred method for implant placement. Lou (Lou et al., 2020) and others conducted a precision analysis involving 50 patients and 96 implants, which demonstrated that digitally guided implant placement ensures accurate implant angulation and positioning while enhancing the precision of the implant’s three-dimensional placement. Similarly, Han (Han X. et al., 2021) performed a clinical control study on 84 patients with missing teeth and confirmed the high accuracy of digitally guided implantation. Consistent findings were also reported by Wang (Wang et al., 2021) and Takács (Takács et al., 2023) using similar experimental methodologies. A critical factor in achieving precise implant placement is whether the digital guide plate can be accurately seated and remain stable during use without unintended displacement. Currently, the placement accuracy of digital guides is assessed visually through an “open window” in the guide, which relies on the clinician’s judgment to determine its fit with the tooth surface. This method is prone to human error and lacks real-time visualization. Additionally, there is no dynamic monitoring system to assess the guide’s stability during use, making it difficult to detect minor prying movements caused by force imbalances. Such undetected displacement can compromise the accuracy of implant placement. Therefore, it is crucial to explore and develop an intelligent digital guide plate capable of real-time visualization and stability detection during seating and use. This advancement would significantly improve the precision and reliability of digitally guided implant procedures.

Mechanoluminescence (ML) materials, which exhibit visible light emission in the presence of external mechanical forces, have the advantages of high brightness, high sensitivity, and a broad stress response range (Wang et al., 2015). Due to these properties, ML materials have been extensively utilized in the development of smart stress sensors and crack detection systems (Olawale et al., 2011; Jeong et al., 2014; Feng and Smet, 2018; Yun et al., 2013). The research group led by Chao-Nan Xu at the National Institute of Advanced Industrial Science and

Technology (AIST), Japan, has engineered an artificial skin employing ZnS: Mn²⁺ piezoelectric mechanoluminescent films. The mechanoluminescence intensity of these films varies in response to applied stress, demonstrating high sensitivity to changes in external pressure. Additionally, the material is reusable, making it a promising candidate for applications in pressure sensing, wearable electronics, and biomedical monitoring (Xu et al., 1999; Wang et al., 2019). Kim et al. Park et al. (2019), Zhang et al. (2017); Zhang et al. (2018), and Jeong et al. (2017) utilized ZnS: Cu/PDMS composite materials to prepare mechanoluminescent basement membrane to provide a frequency selector similar to the human cochlear basement membrane. The incorporation of ZnS: Cu/Mn²⁺ composites with polydimethylsiloxane (PDMS) enables the fabrication of stretchable mechanoluminescent fibers, which can be woven into wearable textiles that emit light in response to mechanical forces generated by motor activities. Jiang et al. (2018) also proposed a method utilizing the mechanoluminescent properties of SrAl₂O₄: Eu²⁺, Dy³⁺ to visualize the distribution of occlusal forces on artificial teeth. By leveraging the occlusal forces within the oral cavity and the force-responsive characteristics of mechanoluminescent materials, this approach enables real-time stress visualization on the surface of dental restorations. This technique facilitates the identification of occlusal high points. The aforementioned experimental results successfully demonstrated the feasibility of detecting clinical artificial tooth occlusion using mechanoluminescent materials. These findings highlight the exceptional sensitivity of mechanoluminescent materials to both friction and pressure. BaSi₂O₂N₂:Eu²⁺ (BSON) oxynitride phosphor offers several advantages, including stable mechanoluminescent properties, high light conversion efficiency, favorable biocompatibility, and environmentally friendly synthesis methods (Zeng et al., 2023). Zhang et al. (2023) was evaluated BSON/PDMS biosafety by cell counting kit-8 (CCK-8), Calcein-AM fluorescent staining, hemolysis, oral mucosal irritation, and acute and subacute systemic toxicity tests. These findings suggested that BSON is biocompatible and suitable for long-term contact with the human body, opening potential applications in dentistry.

Notably, the oral cavity, with its complex environment of continuous friction and mechanical stress, presents a unique challenge. Given these conditions, it is envisioned that integrating mechanoluminescent materials into digital guide plate materials could enable the development of intelligent digital guides. Such an approach would allow real-time stress-induced mechanoluminescence even in low-light or dark environments, addressing key limitations of traditional digital guide plates. Specifically, this innovation would enhance precision in visualizing occlusal force distribution and identifying occlusal high points, thereby improving implant positioning accuracy. Furthermore, it would address the issue of visually monitoring the stability of digital guide plates during their application.

In the present study, mechanoluminescent material (BaSi₂O₂N₂:Eu²⁺, BSON) was introduced into digital guide plate materials, developing an intelligent digital guide plate capable of precise positioning and real-time visualization of dynamic balance during use. The modified BSON digital guide material was characterized using SEM, TEM, and elemental mapping. The chemical composition was analyzed using XRD, FTIR, and XPS. Mechanical properties were evaluated through three-point bending



and compression strength tests, while hydrophilicity was assessed via water contact angle measurements. Mechanoluminescence performance was investigated using spectroscopic analysis, and biocompatibility was determined through Cell counting Kit-8 (CCK-8) assays and LIVE/DEAD staining experiments. In addition, the intelligent digital guide plate's ability to provide real-time visualization of its positioning and dynamic balance was validated in clinical implant cases. Its accuracy in guiding implant placement was systematically assessed, offering robust experimental data to support its clinical application and potential for improving the precision and reliability of implant restoration procedures.

In the present experiment, BM mechanoluminescent guide composites were prepared by means of a mechanical blending method, and their chemical composition, mechanical properties, mechanoluminescent properties, and biocompatibility were subsequently explored. Additionally, the practical application of BM mechanoluminescent guide composites in clinical settings was refined, demonstrating their feasibility for use in implant restorations. A graphical abstract is shown in Figure 1.

2 Materials and methods

2.1 Preparation of $\text{BaSi}_2\text{O}_2\text{N}_2:\text{Eu}^{2+}$ /PMMA with intelligent digital guides

Different proportions (2 wt%, 4 wt%, 8 wt%, 16 wt%, 32 wt%) of BOSN material were mechanically co-mingled with methacrylic acid resin monomer (MAA), respectively, and ultrasonicated for 5 min at room temperature to form the composites, which were recorded as BM2, BM4, BM8, BM16, BM32, respectively, and were reserved for spare use; the BMs were loaded into the $40 \times 4 \times 1$ mm ($L \times W \times H$) and $25 \times 25 \times 2$ mm ($L \times W \times H$) acrylic molds, respectively, and the light-cured samples were used for characterization and analysis; patients with clinical dental defects were selected, and the design of implant guides was completed according to the implantation plan, and with the help of 3D printers (HEYGEARS, ChairSide Pro), the BM with an optimal BOSN ratio was used as the raw material to complete smart digital guides. BM with the optimal BOSN ratio was used as the raw material to complete the printing of the intelligent digital guide plate.

2.2 Characterization

The material was characterized by field emission scanning electron microscopy (SEM, S4800, Hitachi, American), X-ray powder diffraction (XRD, Smart APEX II, BRUKER, German), Fourier transform infrared spectroscopy (FTIR, Spectrum 100, Perkin Elmer, Inc., United States), and X-ray photoelectron spectroscopy (XPS, Axis Supra, SHIMADZU, Japan) were used to characterize the microstructural morphology and chemical composition of the BMs, respectively. A microcomputer-controlled electronic universal testing machine (Transcell Technology inc, BAB-10MT, American) was used to test the mechanical properties of the BMs, and a contact angle meter (KRUSS, Germany) was used to evaluate the hydrophilic properties. The friction mechanoluminescence properties of BM were examined by a friction and wear tester connected to a spectrometer in a dark environment under 100 g, 200 g, 300 g, 400 g, and 500 g of force. The compression mechanoluminescence performance of BM under the force of 300 N was detected by using a microcomputer-controlled electronic universal testing machine connected to a spectrometer in a dark environment.

2.3 Cytocompatibility test

Mouse fibroblasts L929 were selected to evaluate BM biocompatibility. BM samples were immersed in deionized water for 1 day, and after removing the residual impurities on the surface, they were placed in an ultra-clean cell operating table and irradiated by ultraviolet light for 30 min each on the front and back sides. Sterilized BM samples were placed into cell culture dishes, and 8 mL of medium was added to each according to the standard immersion ratio of $3 \text{ cm}^2/\text{mL}$ according to the ISO4900-10933 standard, and then cultured in a cell culture incubator at 37°C with 5% CO_2 saturation humidity after incubation for 1 day. The incubation was continued for 1 day, 2 days, and 4 days. The proliferation of L929 cells was measured using the CCK-8 assay and the relative value-added rate of the cells was calculated. Cell viability was evaluated by live cell staining over the LIVE/DEAD Staining Assay Kit, analyzed and photographed with an inverted microscope (Ti-U, Nikon, Japan).

2.4 Practical application tests

Thirty-seven patients with clinical dental defects were selected, and a total of 50 implants were placed using the intelligent digital guide prepared by BM to guide the implant placement. Digital camera was taken during implantation and analyzed. Cone Beam CT (CBCT) was taken after implantation, and the implant after implantation was overlapped with the virtual implant in the design process of the guide plate, and the implantation accuracy was analyzed by measuring the distance deviation in the proximal and distal mesial, buccolingual and vertical directions. The selection criteria of patients with dental defects are as follows:

2.5 Ethics approval statement

The L929 mouse fibroblast cell line (ATCC[®] CCL-1™) used in this study was obtained from a collaborative research group at the School of Stomatology, Lanzhou University. Its original source is the commercially available cell line from the American Type Culture Collection (ATCC). According to the Guidelines for Ethical Review of Welfare of Laboratory Animals in China and the regulations of the Ethics Committee of the School of Stomatology, Lanzhou University, no additional ethical approval was required for the use of internationally certified standardized cell lines.

2.6 Statistical analysis

SPSS v29 was applied for the statistical analysis. Moreover, univariate analysis of variance and Duncan multiple range test were adopted to examine discrepancies of different groups. $P < 0.05$ was considered to be significant.

3 Results and discussion

3.1 Synthesis and characterization of BM

Figure 2A shows the schematic diagram of the BM preparation and characterization. To evaluate the luminescence performance of the BM, cylindrical samples were fabricated with dimensions of 40 mm in diameter and 1 mm in height, as well as 4 mm in diameter and 6 mm in height, as depicted in Figures 2B,C. The doping ratios of the mechanoluminescent materials were 0 wt%, 2 wt%, 4 wt%, 8 wt%, 16 wt%, and 32 wt%, respectively. It was observed that as the concentration increased, the samples exhibited progressively darker colors, suggesting the successful preparation of all sample groups. To analyze the chemical composition and microstructure of the BM samples, SEM imaging and elemental mapping were conducted. Figure 2D depicts the SEM image of the matrix material alone, namely, PMAA, while Figure 2E illustrates its elemental distribution, indicating the presence of oxygen and carbon. Figure 2F shows the SEM image of the mechanoluminescent material BSON, characterized by irregular rod-shaped particles with diameters ranging from approximately 5–10 μm . Figure 2G provides the elemental mapping of BSON, confirming the presence of oxygen, nitrogen, strontium, and barium. Figure 2H presents the SEM images of BM composites with varying BSON doping concentrations (BM2, BM4, BM8, BM16, and BM32). His findings suggest that upon the introduction of BSON, the initially uniform PMAA matrix transformed into a granular structure with evenly dispersed particles, exhibiting minimal agglomeration. As the doping ratio rose, the granularity of the composite material became augmented. Visualized in Figure 2I are the elemental distributions within the BM composite materials, showcasing the presence of oxygen, carbon, nitrogen, strontium, and barium. This mapping unequivocally confirms the effective embedding of BSON within the PMAA matrix. Such observations corroborate the proficient synthesis of BM composites, yielding rigorously characterized samples tailored for ensuing experimental inquiries.

3.2 Morphological structure of BM

In order to further investigate the morphology and structure of the BM composites, XRD, FTIR, and XPS were used to characterize the composites. Figure 3A shows the FTIR, XRD, and XPS of BSON, PMAA, and BM composites. In the FTIR spectra, the absorption peak at $1,025\text{ cm}^{-1}$ for BSON corresponds to the symmetric stretching vibration of the Si-N bond, while the peak at 842 cm^{-1} represents the symmetric stretching vibration of the Si-O bond (Boulesbaa, 2021). The FTIR spectrum of PMAA that its double peaks at $2,390\text{ cm}^{-1}$ and $2,356\text{ cm}^{-1}$ may originate from the O-H stretching vibrational coupling of the carboxylic acid dimer, while the strong absorption band at $1,722\text{ cm}^{-1}$ corresponds to the characteristic vibrational mode of the ester carbonyl group (C=O). In addition, the absorption at $1,634\text{ cm}^{-1}$ may be related to the stretching vibration of the C=C double bond, the band at $1,425\text{ cm}^{-1}$ can be attributed to the bending vibration of $-\text{CH}_2-$, and the double peaks in the low-wave number region at 642 cm^{-1} and 572 cm^{-1} are suggest complex vibrational coupling of the polymer backbone, as the concentration of BSON increases, the BM composites appear to have wave peaks overlapping their characteristic peaks of BSON that are progressively more pronounced. Figure 3B displays the XPS spectra of PMAA, where the C-C bond splitting peak appears at 284 eV, the C-O bond splitting peak at 286 eV, and the C=O bond splitting peak at 288 eV for carbon. Additionally, oxygen-related peaks include the C-O bond splitting peak at 531 eV and the H-O-C splitting peak at 533 eV. Figure 3C shows the XPS spectra of BSON, revealing an H-O-C splitting peak at 532 eV and a C-O bond splitting peak at 530 eV for oxygen, along with $\text{Ba}3d_{3/2}$ and $\text{Ba}3d_{5/2}$ splitting peaks at 796 eV and 780 eV for barium, respectively. Further, the Si2p characteristic peak appears at 102 eV for silicon, while the N1s characteristic peak can be observed at 397 eV for nitrogen. Figure 3D presents the XPS spectra of BM composites, where the characteristic peaks of PMAA and BSON can be seen, including the C-C bond splitting peak at 284 eV, C-O bond splitting peak at 286 eV, and C=O bond splitting peak at 289 eV for carbon; the C-O bond splitting peak at 532 eV and the H-O-C splitting peak at 533 eV for oxygen; the $\text{Ba}3d_{5/2}$ splitting peak at 779 eV and Ba splitting peak at 795 eV for barium; the Si2p characteristic peak at 102 eV for silicon; and the N1s characteristic peak at 400 eV for nitrogen. These results collectively confirm the successful integration of BSON into the MAA matrix, demonstrating that the BM composites were prepared by mechanical mixing and not by chemical reaction.

3.3 Mechanical properties and contact angle

The mechanical properties were tested using $25\text{ mm} \times 2\text{ mm} \times 2\text{ mm}$ samples. The modulus of elasticity was 51.27 MPa for PMMA, 164.45 MPa for BM2, 232.67 MPa for BM4, 81.99 MPa for BM16, and 80.63 MPa for BM32, which were increased by 220.75%, 353.81%, 59.92%, and 56.39%, respectively (Figure 4A). Figure 4B illustrates the flexural strength of the materials, showing that PMMA exhibited a flexural strength of 6.44 MPa. The BM2 composite achieved 9.14 MPa, representing a 41.93% increase, while BM4 reached 10.96 MPa, marking a 70.19% enhancement.

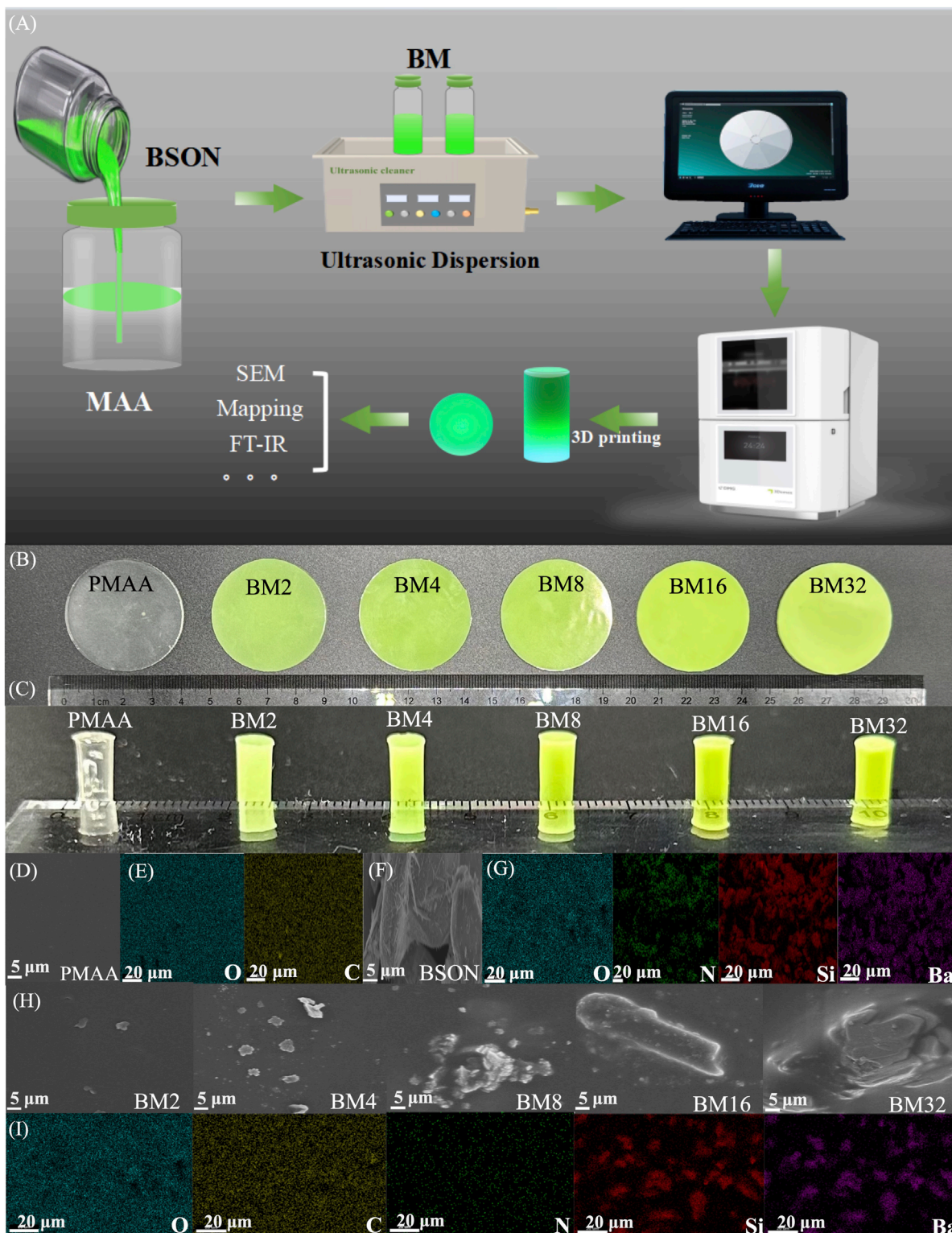


FIGURE 2
(A) Technology roadmap for the preparation of BM samples; **(B)** Friction mechanoluminescence samples of PMAA, BM2, BM4, BM8, BM16, MB32; **(C)** Compression mechanoluminescence samples of PMAA, BM2, BM4, BM8, BM16, MB32; **(D)** SEM of PMAA; **(E)** mapping of PMAA; **(F)** SEM of BSON; **(G)** mapping of BSON; **(H)** SEM of BM2, BM4, BM8, BM16, MB32; **(I)** mapping of BM.

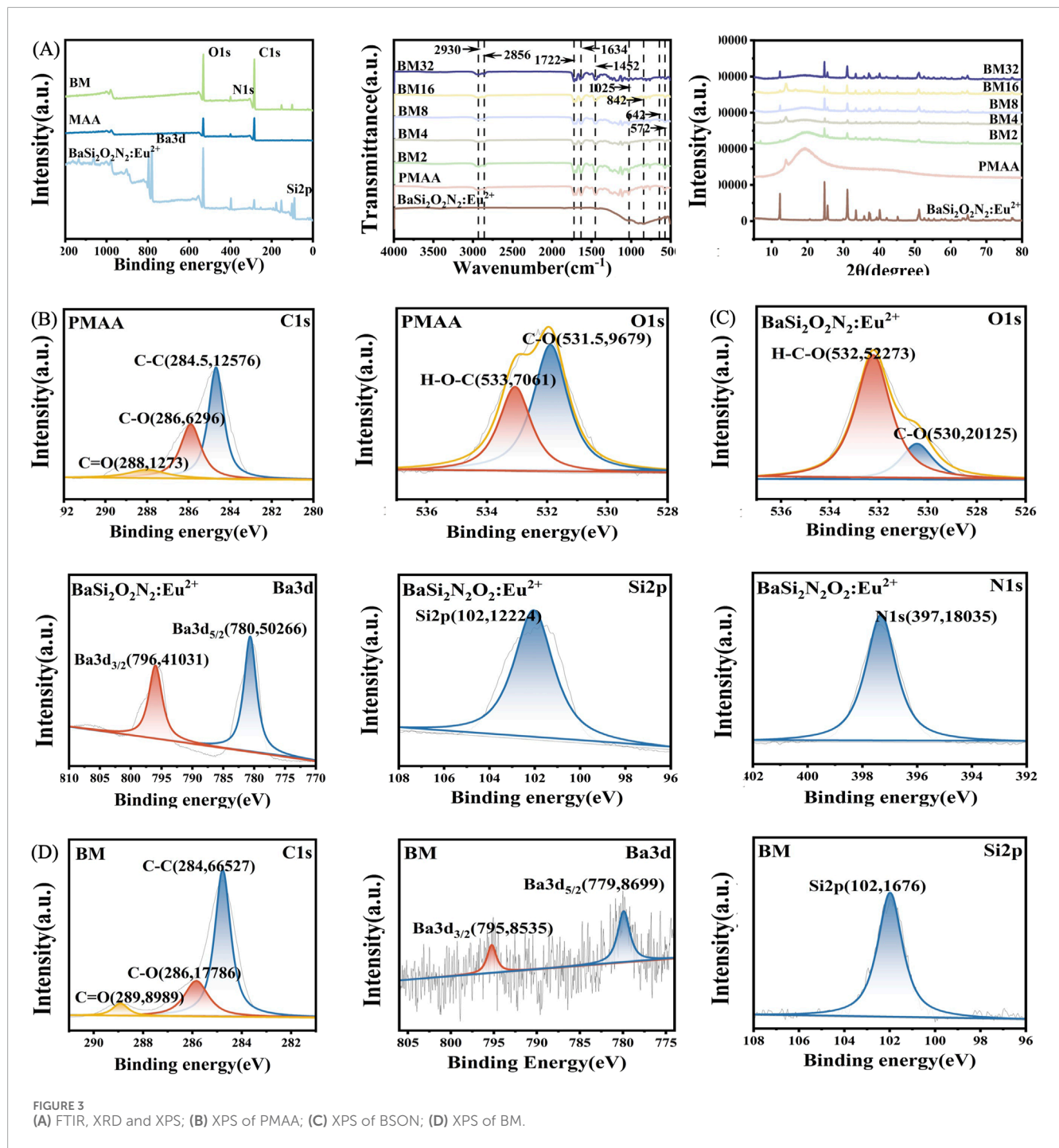
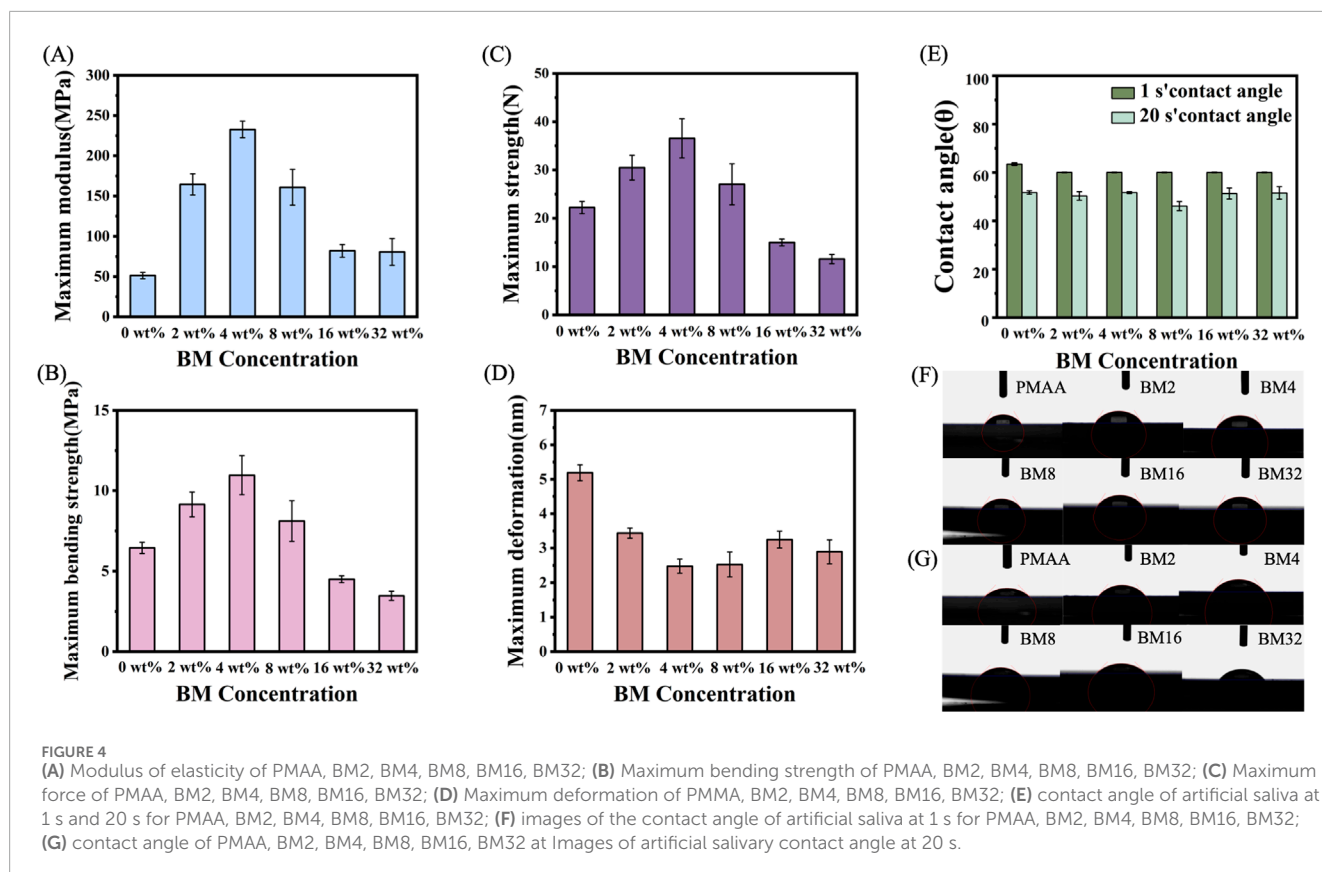


FIGURE 3 (A) FTIR, XRD and XPS; (B) XPS of PMAA; (C) XPS of BSON; (D) XPS of BM.

In contrast, BM8 demonstrated a flexural strength of 8.11 MPa, reflecting a 25.93% increase. However, the values for BM16 and BM32 declined to 4.50 MPa and 3.47 MPa, respectively. Figure 4C presents the maximum force each material could withstand, with PMMA supporting 22.21 N. The BM2 composite withstood 30.47 N, a 37.19% improvement, while BM4 reached 36.54 N, showing a 64.52% increase. BM8 exhibited a maximum force capacity of 27.04 N, an increase of 21.75%, whereas BM16 and BM32 showed reduced load-bearing capacities of 15.01 N and 11.57 N, respectively. Figure 4D illustrates the maximum deformation of each material

after stress application. The largest deformation observed for PMMA was 5.19 nm, whereas BM2 exhibited a reduced deformation of 3.43 nm, representing a 33.91% decrease. BM4 showed the lowest deformation at 2.48 nm, marking a 52.22% reduction, while BM8 exhibited a similar reduction to 2.53 nm, a 51.25% decrease. However, as the BSON concentration continued to increase, the deformation values rose slightly, with BM16 at 3.25 nm (a 37.38% reduction) and BM32 at 3.89 nm (a 25.05% reduction). As the concentration of BSON increased, the mechanical properties of BM composites improved compared to PMMA. The enhancement in



mechanical performance can be attributed to several mechanisms: (1) Particle reinforcement effect: the mechanoluminescent material, dispersed as rigid particles within the resin matrix, enhances the composite's mechanical strength through a reinforcement mechanism (Fu et al., 2000). (2) Interfacial interactions: a strong interfacial bond between the mechanoluminescent material and the resin matrix allows for efficient stress transfer, thereby improving overall strength (Bian et al., 2021). (3) Increased cross-linking density: the force-emitting material may act as a cross-linking point or facilitate cross-linking reactions within the resin matrix, further strengthening the composite (Hussain et al., 2006). (4) Optimization of stress distribution: the incorporation of force mechanoluminescent materials helps to reduce stress concentrations, minimizing weak points and improving structural integrity (Wetzel et al., 2002). With increasing BSON concentration, the elastic modulus, maximum force, and bending strength initially increased, peaking at 4 wt%, before declining. Similarly, the maximum deformation initially decreased, reaching its lowest value at 4 wt%, before increasing again. This trend can be explained by several factors: (1) Filler agglomeration effect: when the concentration of mechanoluminescent material exceeds a certain threshold (e.g., 4 wt%), particles tend to agglomerate, leading to stress concentrations and interfacial defects, which reduce the mechanical strength of the composite. This agglomeration disrupts the homogeneity of the material and serves as an initiation point for cracks under stress (Han Y. et al., 2021). (2) Decrease in interfacial bonding strength: at higher filler concentrations, the interfacial bonding between the resin matrix and the filler may

become uneven or weakened. When the filler concentration is too high, the resin matrix cannot completely encapsulate the filler particles, reducing interfacial bonding strength and, consequently, mechanical performance (Fu et al., 2000). (3) Disruption of the resin matrix continuity: excessive filler concentration may disrupt the structural continuity of the resin matrix, leading to a loss of material integrity. This weakens the load-bearing capacity of the composite. (4) Stress concentration effect: a high filler concentration causes an uneven stress distribution within the composite, leading to stress concentration points that can initiate crack propagation under mechanical load, reducing mechanical strength. These findings indicate that BM composites exhibited optimal mechanical properties when the force mechanoluminescent material concentration was at 4 wt%. Figures 4E–G illustrate the contact angles of PMMA, BM2, BM4, BM16, and BM32 on (Wetzel et al., 2002)artificial saliva at the first and 20th seconds, all of which are less than 90°, demonstrating good hydrophilicity. Further, the hydrophilicity of the samples remains largely unchanged with increasing mechanoluminescent material concentration, suggesting that the addition of these materials does not significantly affect the resin's hydrophilic properties.

3.4 Mechanoluminescence performance

BSON is a force-induced mechanoluminescent material that can be used to monitor the dynamic stability of a guide plate

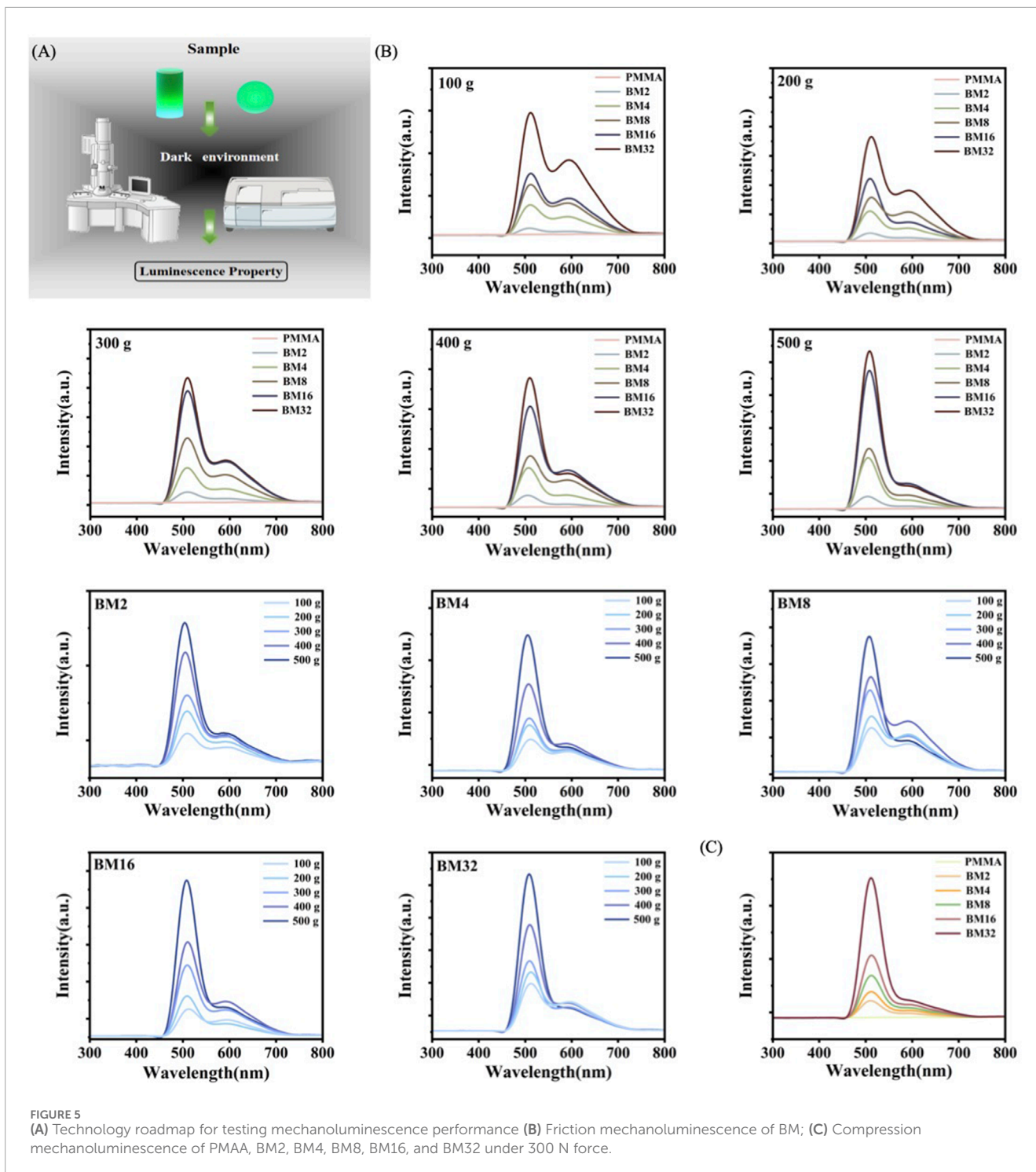


FIGURE 5 (A) Technology roadmap for testing mechanoluminescence performance (B) Friction mechanoluminescence of BM; (C) Compression mechanoluminescence of PMAA, BM2, BM4, BM8, BM16, and BM32 under 300 N force.

when positioned, utilizing its mechanoluminescent response to mechanical stress. The mechanoluminescent performance of the samples was evaluated using a spectrometer, with friction mechanoluminescence tested on samples measuring 40 mm in diameter and 1 mm in height, connected to a friction wear instrument in a dark environment. Figures 5A, B₁₋₅ show the mechanoluminescence of PMAA and BM composites under forces of 100 g, 200 g, 300 g, 400 g, and 500 g, demonstrating that the mechanoluminescence intensity increased with the

addition of BSON content under the same force. Figure 5B₆₋₁₀ display the mechanoluminescence of BM2, BM4, BM8, BM16, and BM32 under the same range of forces, where the mechanoluminescence intensity increased as the applied force increased, regardless of the composite material. Figure 5C presents the compression-induced mechanoluminescence of PMAA, BM2, BM4, BM8, BM16, and BM32 under a 300 N load, measured with a microcomputer-controlled electronic universal testing machine connected to the spectrometer in a dark environment.

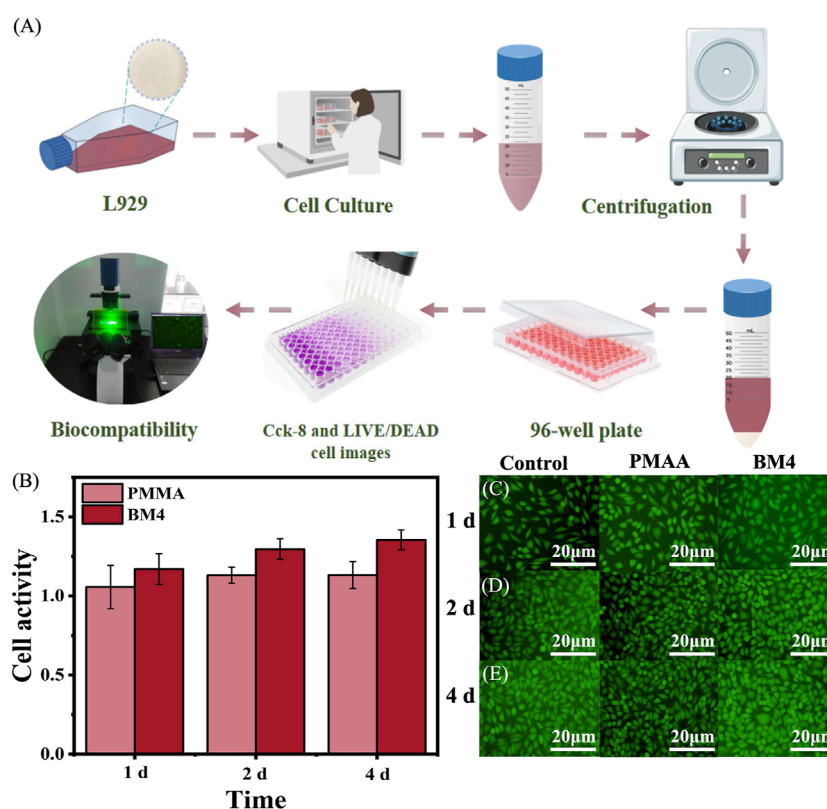


FIGURE 6 (A) Technical roadmap for cytocompatibility assays (B) Cellular activity of PMAA and BM4, on days 1, 2, and 4; (C) Live cell staining of control, PMAA and BM4 on day 1; (D) Live cell staining of control, PMAA and BM4 on live cell staining on day two; (E) control, PMAA and BM4 live cell staining on day four.

As the concentration of force-induced mechanoluminescent material increased, the mechanoluminescence effect became more pronounced. These results indicate that, when combined with BSON, retained the mechanoluminescence effect of BSON under stress, highlighting the potential for the practical application of BM composite guide plate materials in clinical settings.

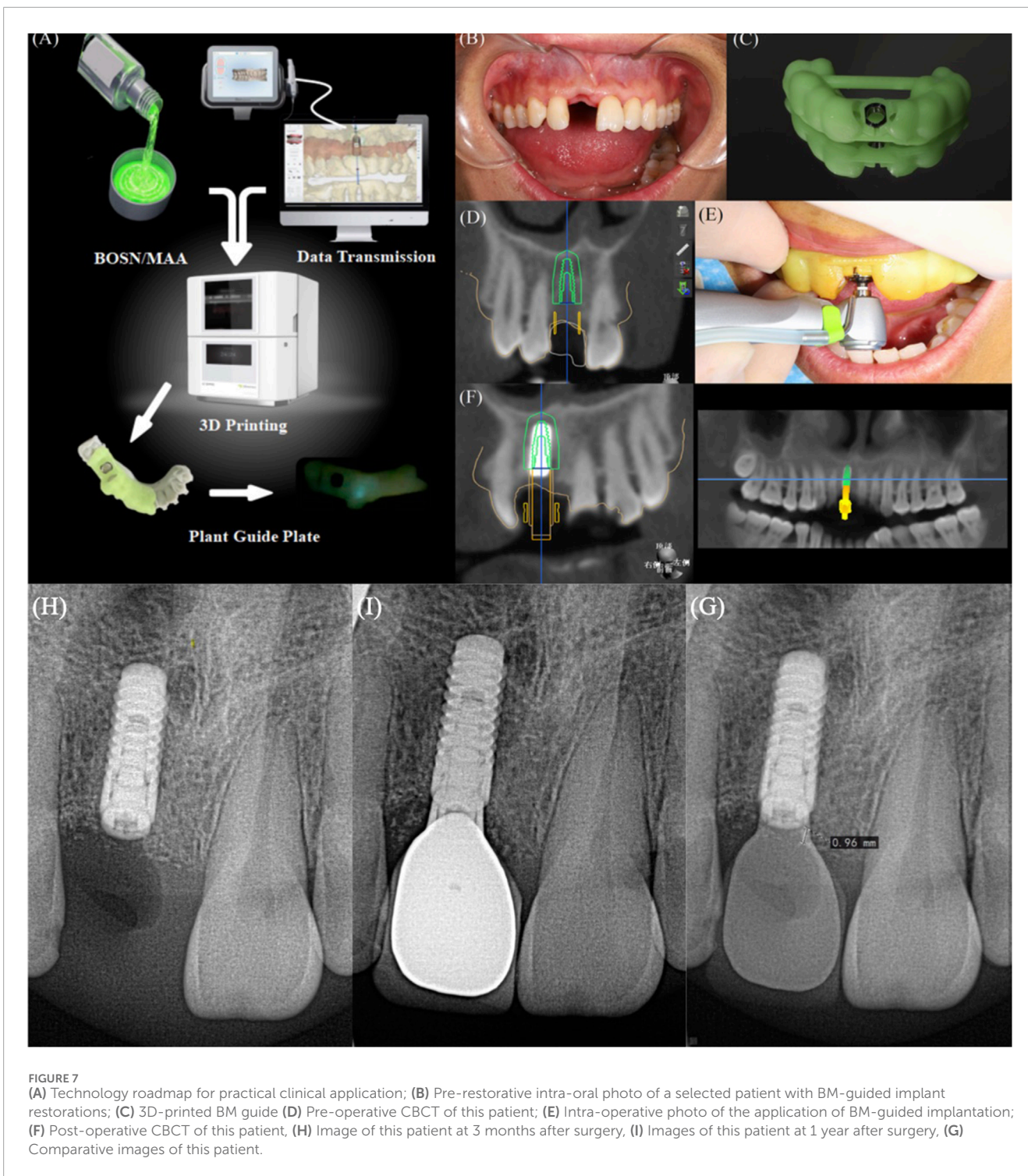
3.5 Biocompatibility

The BM4 group demonstrating optimal mechanical properties was selected for biocompatibility evaluation. Following the established methodology, mouse fibroblasts were co-cultured with BM composite extracts to assess their biocompatibility. Cell viability and proliferation were assessed using the CcK-8 assay and LIVE/DEAD staining on days 1, 2, and 4 of culture. Figures 6A, B presents the results of the quantitative CcK-8 assay after 1, 2, and 4 days of culture. This assay assessed the cellular viability of PMMA and BM composites. On days 1, 2, and 4, the cell activity of PMMA was 1.06, 1.31, and 1.32, respectively, while BM4 recorded 1.17, 1.30, and 1.35. Notably, the groups exhibited a significant enhancement in cell growth on day 1, 2 and 4 than PMMA groups. Over time, cell activity increased steadily in the PMMA and BM4 groups, the absorbance remained above 0.75 across all samples, meeting 10,993-5:2009 standard, which confirms that the

composites are non-toxic and biocompatible. Figures 5C–E display the fluorescence staining images of live cells in PMAA and BM4 on days 1, 2, and 4, respectively. The results indicate that L929 cells cultured with BM composites exhibited notable adhesion and proliferation, aligning with the quantitative CcK-8 findings. These observations confirm that BM composites possess biocompatibility and, due to their non-toxic properties, can be considered suitable for practical clinical applications in dental implant restoration.

3.6 Practical application

Currently, real-time dynamic detection of implant positioning and stability during implant placement is not feasible in clinical practice. To address this issue, incorporating mechanoluminescent materials into the guide plate material offers a potential solution by enabling visualization of implant positioning and stability. Based on experimental results, the BM composite with a 4 wt% concentration exhibited optimal mechanical properties and biocompatibility. Its superior mechanical strength, stability, and cytocompatibility make it the most suitable choice for clinical application. Therefore, the 4 wt% BM composite material was selected for further implementation in clinical implant procedures to enhance precision and reliability in implant placement.



3.7 Clinical cases

Figure 7A presents a process flow schematic detailing the BM implant guide fabrication. A clinical case of an anterior 11 implant placement was conducted using a BM composite implant guide (Figure 7B). Preoperatively, 3-Shape software was utilized to design the guide, and the printing of the BM composite implant guide was completed using Black Grid 3D printing equipment. Figure 7C

presents the BM composite guide printed using a Hegger 3D printer prior to the patient’s implant surgery, confirming its printability and structural consistency with conventional implant guides. Before the procedure, the BM composite implant guide was trial-fitted and examined to ensure proper adaptation. Sterilization was carried out by soaking the guide in iodine vapor, followed by routine disinfection and local anesthesia administration. The implant surgery was performed under the guidance of the BM composite

TABLE 1 Inclusion criteria and Guidelines followed for patient selection.

Category	Criteria	Guidelines followed
Age	18–65 years	ITI Consensus Guidelines, STROBE Guidelines
Systemic Health	ASA I or II classification (healthy or mild systemic disease without functional limitations)	
Dental Defect Type	Single or multiple tooth loss in the maxillary or mandibular arch	
Bone Volume	Adequate bone volume for implant placement: Bone height ≥ 10 mm, Bone width ≥ 5 mm	
Bone Quality	Bone density sufficient for primary implant stability (assessed via CBCT)	
Oral Health	No active infections or pathological conditions in the implant site	
Compliance	Willingness to participate in the study and provide informed consent	
Exclusion of Risk Factors	No history of radiation therapy in the head and neck region, No severe systemic diseases (e.g., uncontrolled diabetes, osteoporosis), No heavy smoking (≥ 10 cigarettes per day) or parafunctional habits (e.g., bruxism)	

TABLE 2 50 cases of BM composite implant guide error.

Near- and Far-midrange error (mm)	Buccolingual error (mm)	Depth error (mm)
0.505 \pm 0.073	0.392 \pm 0.037	0.710 \pm 0.028

implant guide, with intraoperative photographs taken to document the process (Figures 7D,E). Postoperatively, CBCT imaging was acquired and imported into 3-Shape software in “.dicom” format for analysis of implant placement accuracy (Figure 7F). The results provided insight into the clinical feasibility and precision of the BM composite implant guide in guided implant surgery. Postoperative radiographic evaluation of bone resorption following implant placement was performed at 3 months and 1 year, with comparative measurements documented in Figures 7G,H.

In the present clinical study, a total of 50 patients requiring implant restorations were randomly selected, and BM composite implant guides were utilized during surgery. Preoperative and postoperative CT images were acquired to evaluate the accuracy of implant placement. As shown in Table 1, the analysis revealed no significant difference in the overall error when compared to traditional implant guides. These results indicate that BM composite implant guides provide comparable precision to conventional guides, demonstrating their feasibility for clinical application. The observations imply that BM composite implant guides can be effectively implemented in guided implant surgeries, supporting their potential for widespread clinical adoption. The results of a 1-year follow-up of 12 patients are shown in Table 2, which shows that after BM4-guided implantation, the mean bone resorption was

0.96 \pm 0.13 mm, which meets the established criterion of less than 0.25 mm per year within 5 years after implantation.

4 Conclusion

In conclusion, we successfully blended the mechanoluminescent material BSON with the guide material MAA by ultrasonication to prepare a BSON/PMMA composite and verify its mechanical, mechanoluminescent, and biocompatibility properties. The results show that BM4 has excellent mechanical properties, with its modulus of elasticity, maximum force, and bending strength enhanced by 353.81%, 64.52%, and 70.19%, respectively, compared with PMMA, and the maximum size variable reduced by 51.25% compared with PMMA; the cell viability is greater than 75%, and it has good biocompatibility. In addition, the BM composite implant guide was obtained by 3D printing technology, which proved that the implant guide was able to exist visible light under stress, and it was a kind of implant guide that could be used in clinical implant restoration surgery, which provided more solid data support for the development of precise digital medical technology, and made the implant restoration technology develop in the direction of more precise, minimally invasive, and predictable clinical results. The BM

composite implant guide solves the problems of precise positioning of the intelligent digital guide and visualization and detection of stability in the process of using it, and provides more solid data support for the development of precise digital medical technology, so that the implant restoration technology develops in the direction of more precise, minimally invasive, and predictable clinical results.

Data availability statement

The raw data supporting the conclusions of this article will be made available by the authors, without undue reservation.

Ethics statement

The studies involving humans were approved by the School of Stomatology Lanzhou University (LZUKQ-2022-094). The studies were conducted in accordance with the local legislation and institutional requirements. Written informed consent for participation was not required from the participants or the participants' legal guardians/next of kin because The clinical data involved in this experiment have been fully anonymized.

Author contributions

X-ZZ: Data curation, Methodology, Writing – original draft, Writing – review and editing. N-YS: Data curation, Methodology, Writing – original draft, Writing – review and editing. QC: Methodology, Writing – original draft. YX: Methodology, Writing – original draft. Y-ZG: Writing – original draft. M-ZH: Writing – original draft. F-XS: Funding acquisition, Supervision, Writing – review and editing. BL: Funding acquisition, Supervision, Writing – review and editing.

References

- Abad-Coronel, C., Vandeweghe, S., Cervantes, M. D. V., Lara, M. J. T., Córdova, N. M., and Aliaga, P. (2024). Accuracy of implant placement using digital prosthetically-derived surgical guides: a systematic review. *Appl. Sci.* 14 (16), 7422. doi:10.3390/app14167422
- Beck, J. D., Youngblood, M., Atkinson, J. C., Mauriello, S., Kaste, L. M., Badner, V. M., et al. (2014). The prevalence of caries and tooth loss among participants in the Hispanic Community Health Study/Study of Latinos. *J. Am. Dent. Assoc.* 145 (6), 531–540. doi:10.14219/jada.2014.25
- Bian, J., Han, Y., Wang, F., Liu, B., Li, H., and Wang, Z. (2021). Enhanced mechanoluminescence of ZnS:Mn²⁺ in flexible polyurethane via interfacial interactions. *Mat. Res. Bull.* 140, 111295. doi:10.1016/j.matresbull.2021.111295
- Boulesbaa, M. (2021). "Spectroscopic ellipsometry and FTIR characterization of annealed SiO_xNy:H films prepared by PECVD." *Opt. Mater.* 122: 111693. doi:10.1016/j.optmat.2021.111693
- Feng, A., and Smet, P. F. (2018). A review of mechanoluminescence in inorganic solids: compounds, mechanisms, models and applications. *Materials* 11 (4), 484. doi:10.3390/ma11040484
- Fu, S. Y., Lauke, B., Mäder, E., Yue, C. Y., and Hu, X. (2000). "Tensile properties of short-glass-fiber- and short-carbon-fiber-reinforced polypropylene composites." *Compos. Part A Appl. Sci. Manuf.* 31 (10): 1117–1125. doi:10.1016/S1359-835X(00)00068-3
- Han, X., Qi, C., Guo, P., Zhang, S., Xu, Y., Lv, G., et al. (2021). Whole-process digitalization-assisted immediate implant placement and immediate restoration in the aesthetic zone: a prospective study. *Med. Sci. Monit.* 27, e931544. doi:10.12659/MSM.931544
- Han, Y., Bai, Y., Bian, J., Guo, X., Liu, B., and Wang, Z. (2021). "Polydimethylsiloxane-based mechanoluminescent occlusal splint with the visualization of occlusal force." *ACS Appl. Polym. Mater.* 3 (10): 5180–5187. doi:10.1021/acsapm.1c00917
- Hussain, F., Hojjati, M., Okamoto, M., and Gorga, R. E. (2006). "Review article: polymer-matrix nanocomposites, processing, manufacturing, and application: an overview." *J. Compos. Mater.* 40 (17): 1511–1575. doi:10.1177/0021998306067321
- Jeong, S. M., Song, S., Joo, K. I., Kim, J., Hwang, S. H., Jeong, J., et al. (2014). Bright, wind-driven white mechanoluminescence from zinc sulphide microparticles embedded in a polydimethylsiloxane elastomer. *Energy & Environ. Sci.* 7 (10), 3338–3346. doi:10.1039/c4ee01776e
- Jeong, S. M., Song, S., Seo, H.-J., Choi, W. M., Hwang, S.-H., Lee, S. G., et al. (2017). "Smart fibers: battery-free, human-motion-powered light-emitting fabric: mechanoluminescent textile (adv. Sustainable syst. 12/2017)." *Adv. Sustain. Syst.* 1 (12). doi:10.1002/adsu.201770121
- Jiang, Y., Wang, F., Zhou, H., Fan, Z., Wu, C., Zhang, J., et al. (2018). Optimization of strontium aluminate-based mechanoluminescence materials for occlusal examination of artificial tooth. *Mater. Sci. Eng. C Mater. Biol. Appl.* 92, 374–380. doi:10.1016/j.msec.2018.06.056
- Li, K., Liu, F., Liu, P., Wei, C., and Li, X. (2023). Clinical effect and aesthetic evaluation of minimally invasive implant therapy. *Emerg. Med. Int.* 2023, 9917311–9917317. doi:10.1155/2023/9917311
- Lou, F. Z., Zhang, M. R., Rao, P. C., Luo, S. H., Tang, M. Y., and Xiao, J. G. (2020). Precise investigation of digital guide plates applied to implant surgery of anterior teeth. *Hua Xi Kou Qiang Yi Xue Za Zhi* 38 (2), 170–176. doi:10.7518/hxkq.2020.02.011

Funding

The author(s) declare that financial support was received for the research and/or publication of this article. This research was funded by National Natural Science Foundation of China (82370926); Key Research and Development Program of Gansu Province (22YF7FA016); Science and Technology Project of Lanzhou (2024-4-28); Lanzhou University (lzukqky-2022-t18,071100163, 071100232, 20220850, 20220820, lzukqky-2023-q03).

Conflict of interest

The authors declare that the research was conducted in the absence of any commercial or financial relationships that could be construed as a potential conflict of interest.

Generative AI statement

The author(s) declare that no Generative AI was used in the creation of this manuscript.

Publisher's note

All claims expressed in this article are solely those of the authors and do not necessarily represent those of their affiliated organizations, or those of the publisher, the editors and the reviewers. Any product that may be evaluated in this article, or claim that may be made by its manufacturer, is not guaranteed or endorsed by the publisher.

- Nulty, A. (2024). A literature review on prosthetically designed guided implant placement and the factors influencing dental implant success. *Br. Dent. J.* 236 (3), 169–180. doi:10.1038/s41415-024-7050-3
- Olawale, D. O., Dickens, T., Sullivan, W. G., Okoli, O. I., Sobanjo, J. O., and Wang, B. (2011). Progress in triboluminescence-based smart optical sensor system. *J. Luminescence* 131 (7), 1407–1418. doi:10.1016/j.jlumin.2011.03.015
- Park, H. J., Kim, S. M., Lee, J. H., Kim, H. T., Seung, W., Son, Y., et al. (2019). Self-powered motion-driven triboelectric electroluminescence textile. *ACS Appl. Mater. Interfaces*, 1–26. doi:10.1021/acsami.8b16023
- Peng, K., Zhou, Y., Dai, Y., Wang, Q., Hu, Y., and Dai, Q. (2021). The effect of denture restoration and dental implant restoration in the treatment of dentition defect: a systematic review and meta-analysis. *Ann. Palliat. Med.* 10 (3), 3267–3276. doi:10.21037/apm-21-421
- Peres, M. A., Macpherson, L. M. D., Weyant, R. J., Daly, B., Venturelli, R., Mathur, M. R., et al. (2019). Oral diseases: a global public health challenge. *Lancet* 394 (10194), 249–260. doi:10.1016/S0140-6736(19)31146-8
- Takács, A., Hardi, E., Navarro Cavalcante, B. G., Szabó, B., Kispélyi, B., Joób-Fancsaly, Á., et al. (2023). “Advancing accuracy in guided implant placement: a comprehensive meta-analysis.” *J. Dent.* 139: 104748. doi:10.1016/j.jdent.2023.104748
- Wang, X., Zhang, H., Yu, R., Dong, L., Peng, D., Zhang, A., et al. (2015). Dynamic pressure mapping of personalized handwriting by a flexible sensor matrix based on the mechanoluminescence process. *Adv. Mater.* 27 (14), 2324–2331. doi:10.1002/adma.201405826
- Wang, X. P., DengfengHuang, B. P., CaofengWang, Z. L., and Wang, Z. L. (2019). Piezophotonic effect based on mechanoluminescent materials for advanced flexible optoelectronic applications. *Nano Energy* 55, 389–400. doi:10.1016/j.nanoen.2018.11.014
- Wang, Z., Liu, J., Wang, X., Wang, N., and Teng, M. (2021). Effect of CAD/CAM guide plate combined with socket-shield technique in immediate implantation of anterior teeth aesthetic area and its influence on aesthetics. *Front. Surg.* 8, 833288. doi:10.3389/fsurg.2021.833288
- Wetzel, B., Hauptert, F., Friedrich, K., Zhang, M. Q., and Rong, M. Z. (2002). “Impact and wear resistance of polymer nanocomposites at low filler content.” *Polym. Eng. & Sci.* 42 (9): 1919–1927. doi:10.1002/pen.11084
- Xu, C. N., Watanabe, T., Akiyama, M., and Zheng, X. G. (1999). Artificial skin to sense mechanical stress by visible light emission. *Appl. Phys. Lett.* 74 (9), 1236–1238. doi:10.1063/1.123510
- Yun, G. J., Reza Rahimi, M., Gandomi, A. H., Lim, G. C., and Choi, J. S. (2013). Stress sensing performance using mechanoluminescence of SrAl₂O₄:Eu (SAOE) and SrAl₂O₄:Eu, Dy (SAOED) under mechanical loadings. *Smart Mater. Struct.* 22 (5), 055006. doi:10.1088/0964-1726/22/5/055006
- Zeng, Yi, Guo, F., Rao, G.-H., Zhao, J.-T., and Zhang, Z.-J. (2023). High CRI white light-emitting phosphor-in-glass film for laser lighting applications by adding cyan phosphor BaSi₂O₂N₂:Eu²⁺. *Ceram. Int.* 49 (5), 7927–7934. doi:10.1016/j.ceramint.2022.10.302
- Zhang, J., Bao, L., Lou, H., Deng, J., Chen, A., Hu, Y., et al. (2017). Flexible and stretchable mechanoluminescent fiber and fabric. *J. Mater. Chem. C* 5, 8027–8032. doi:10.1039/C7TC02428B
- Zhang, Z., Cui, L., Shi, X., Tian, X., Wang, D., Gu, C., et al. (2018). Textile display for electronic and brain-interfaced communications. *Adv. Mater.* 30 (18), e1800323–e1800323.8. doi:10.1002/adma.201800323
- Zhang, Z., Zong, M., Liu, J., Ren, J., Liu, X., Zhang, R., et al. (2023). Biosafety evaluation of BaSi₂O(2)N(2):Eu(2+)/PDMS composite elastomers. *Front. Bioeng. Biotechnol.* 11, 1226065. doi:10.3389/fbioe.2023.1226065
- Zhi, Q. H., Zhou, Y., Tao, Y., Wang, X., Feng, X. P., Tai, B. J., et al. (2018). Factors impacting the oral health-related quality of life in Chinese adults: results from the 4th national oral health survey. *Chin. J. Dent. Res. official J. Sci. Sect. Chin. Stomatological Assoc. (CSA)* 21 (4), 259–265. doi:10.3290/j.cjdr.a41084